

The Effects of Asymmetric Salt and a Cylindrical Macroion on Charge Inversion: Electrophoresis by Molecular Dynamics Simulations

Motohiko Tanaka

National Institute for Fusion Science, Toki 509-5292, Japan

(Dated: July 31, 2003)

The charge inversion phenomenon is studied by molecular dynamics simulations, focusing on size and valence asymmetric salts, and a threshold of surface charge density for charge inversion. The charge inversion criteria by the electrophoretic mobility and the radial distribution functions of ions coincide except around the charge inversion threshold. The reversed electrophoretic mobility increases with the ratio of coion to counterion radii a^-/a^+ , while it decreases with the ratio of coion to counterion valences Z^-/Z^+ . The monovalent salt enhances charge inversion of a strongly charged macroion at small salt ionic strength, while it reduces reversed mobility otherwise. A cylindrical macroion is more persistent to monovalent salt than a spherical macroion of the same radius and surface charge density.

PACS numbers: 61.25.Hq, 82.45.-h, 82.20.Wt

I. INTRODUCTION

The phenomenon of reverting the charge sign of large ions due to other ions and salts in water solution was known to physical chemists as charge inversion or over-screening for half a century [1]. More recently, it also attracted a significant attention of physicists [2, 3, 4, 5, 6, 7, 8, 9, 10, 11, 12, 13, 14, 15, 16, 17]. Charge inversion is now understood to be the generic phenomenon that occurs in strongly correlated charged systems. It has far reaching consequences in biological and chemical worlds. In particular, it seems to be a decisive ingredient in modern gene therapy, facilitating the delivery of genes (negatively charged DNA) through cell walls of predominantly negative potentials [18, 19].

In our previous papers, we adopted the static [12] and dynamical [13] models to study charge inversion of the spherical macroion by molecular dynamics simulations. In the former study where a macroion was immovable, the static quantities were obtained including the radial distribution profiles of counterions and coions moving in the Langevin thermostat. Generally speaking, the radial profiles of charge density and integrated charge are good indices of charge inversion. However, it is not so when the charge inversion is around the threshold (a counterexample is Fig.4(b) of this paper). Namely, those ions forming the outskirts of the radial distribution profile are not electrostatically bound to the macroion complex and are left behind when the complex moves in the solution. To separate the bound ions from the floating ones, the electrophoretic mobility problem in the explicit (particle) solvent was studied in the latter. We showed that a macroion satisfying the charge inversion conditions drifted with adsorbed counterions and coions toward the external electric field, the direction of which agreed with the sign of inverted charge.

This paper adopts the dynamical (electrophoresis) model and focus on the following points. First, we address the asymmetry effects of the size and valence of counterions and coions. The radii of bare halogen atoms

are large compared to those of alkaline metals, which become eventually larger than the former after hydration. Secondly, we examine the charge inversion threshold in terms of the surface charge density and monovalent salt for the macroions of spherical and cylindrical shapes [20]. The adsorption of cylindrical macroions to a charged surface was previously studied [8, 10]. Instead, we deal with the charge inversion of a cylindrical macroion by adsorption of counterions in the presence of monovalent salt. The cylindrical macroion is shown to be more persistent to monovalent salt than the spherical macroion of the same radius and surface charge density.

In the dynamical study [13], the average static quantities including the radial distribution profiles of ions and the structure of the electrical double layer are not altered in the zeroth order as far as the applied electric field E is much smaller than the electric field produced by the macroion charge, $E \ll Q_0/\epsilon R_0^2$, which is a huge electric field 10⁶V/cm realized by high-power short pulse lasers. Here, Q_0 and R_0 are macroion bare charge and radius, respectively. We have confirmed this by excellent agreement of the integrated charge profiles between the runs with and without the applied electric field, in 3% accuracy for equal-sized coions and trivalent counterions with the parameters of Fig.2 in Sec.3. The net charge of the macroion complex Q^* can be estimated if one makes use of the force balance relation,

$$Q^*E - \nu V \approx 0, \text{ or } Q^* \approx \nu\mu, \quad (1)$$

where $\mu = V/E$ is the measured electrophoretic mobility and ν is the solvent friction. However, one needs to assume the friction for this conversion. The friction that acts on the charged object in charge-neutral electrolyte solution is an enhanced one compared to the Stokesian friction because the velocity decay length is drastically shortened by screening of hydrodynamic interactions [21, 22]. Despite of this uncertainty, the observed mobility agreed qualitatively well with the net charge scaling derived by theory [10].

Other issue of the dynamical study is that the Joule

heat is produced by the applied electric field, which is transferred to background neutral particles through collisions with the ions. To drain the heat, we adopt a heat bath at the domain boundary that is kept at a constant temperature T . The thermal bath screens hydrodynamic interactions and nullifies the momentum of the system on time average. However, it is emphasized that the electric field does not bring in momentum into the charge-neutral system, and that hydrodynamic interactions are weak compared to the electrostatic forces and screened at short distances in the electrolyte solution [21, 22]. Momentum is not transported beyond this distance from the macroion toward the domain boundaries. We confirmed this fact by comparing the mobilities of two runs with and without the heat bath (before heating became significant), the results of which agreed very well within simulation errors (cf. Fig.5 of [13]). Thus, the heat bath does not affect our simulations.

This paper is organized as follows. The simulation method and parameters are described in Sec.II. The effects of asymmetric radii and valences of coions and counterions on the charge inversion phenomenon are studied in Sec.III. The dynamical and static observables, i.e. electrophoretic mobility and radial distribution functions of ions, are compared for the same runs, where good correspondences are found except around the charge inversion threshold. In Sec.IV, the effects of monovalent salt that exits as the base of the Z:1 counterions and coions are examined. There, a cylindrical *infinite* macroion (occupying full length across the domain) that can adsorb geometrically more counterions than a spherical macroion of the same radius is introduced. The cylindrical macroion is found to be more persistent to monovalent salt than the spherical macroion of the same radius and surface charge density. Sec.V will be a summary of this paper.

II. SIMULATION METHOD AND PARAMETERS

Simulation method and parameters for the present study are described here. We take the system consisting of one macroion, many counterions, coions and neutral particles. We solve the Newton equations of motion for each particle with the Coulombic and Lennard-Jones potential forces under a uniform applied electric field E ($E > 0$). A large number of neutral particles are used to model the solvent of given temperature and to treat the interactions among the finite-size macroion, counterions and coions.

The units of length, charge and mass are, a , e , and m , respectively. As is mentioned below, our choice of the temperature corresponds to $a \sim 1.4\text{\AA}$ in water and $m \sim 40$ a.m.u. A spherical macroion with radius $R_0 = 5a$, negative charge Q_0 between $-15e$ and $-81e$, and mass $200m$ is surrounded by the N^+ number of counterions of a positive charge Z^+e and the N^- coions of a negative charge $-Z^-e$. The corresponding surface charge density

of the macroion is between $\sigma_{sp} = 0.048e/a^2$ (0.39 C/m^2) and $0.26e/a^2$ (2.1 C/m^2). A rod-shaped macroion is also used in Sec.IV whose surface charge density is between $\sigma_{rod} = 0.04e/a^2$ (0.33 C/m^2) and $0.08e/a^2$ (0.66 C/m^2). The system is maintained in overall charge neutrality, $Q_0 + N^+Z^+e - N^-Z^-e = 0$. The radii of counterions and coions are a^+ and a^- , respectively, with the counterion radius being fixed at $a^+ = a$, and the radius of neutral particles is $a/2$. The mass of the coions and counterions is m , and that of N_* neutral particles is $m/2$, where we have in mind the water molecule against that of K^+ or Ca^{2+} ions. However, the mass is not involved as far as an equilibrium state is concerned. Approximately one neutral particle is distributed in every volume element $(2.1a)^3 \approx (3\text{\AA})^3$ inside the simulation domain, excluding the locations already occupied by ions, which typically yields 4000 neutral particles for the spherical macroion of radius $R_0 = 5a$. These particles are placed in a cubic box of size $L = 32a$, with periodic boundary conditions in all three directions.

Calculation of the Coulomb forces under the periodic boundary conditions requires the charge sum in the first Brillouin zone and their infinite number of mirror images (the Ewald sum[23]). The sum is calculated with the use of the PPPM algorithm [24, 25]. We use $(32)^3$ spatial meshes for the calculation of the reciprocal space contributions to the Coulomb forces, with the choice of the Ewald parameter $\alpha \approx 0.262$ and the cutoff length $10a$.

In addition to the Coulomb forces, the volume exclusion effect among particles is introduced through the repulsive Lennard-Jones potential $\phi_{LJ} = 4\epsilon[(A/r_{ij})^{12} - (A/r_{ij})^6]$ for $r_{ij} = |\mathbf{r}_i - \mathbf{r}_j| \leq 2^{1/6}A$, and $\phi_{LJ} = -\epsilon$ otherwise to exclude the attraction part. Here \mathbf{r}_i is the position vector of the i -th particle, and A is the sum of the radii of two interacting particles. We relate ϵ with the temperature by $\epsilon = k_B T$, and choose $k_B T = e^2/5\epsilon a$ (we assume spatially homogeneous dielectric constant ϵ). The Bjerrum length is thus $\lambda_B = e^2/\epsilon k_B T = 5a$, which implies $a \approx 1.4\text{\AA}$ in water.

The initial states of the runs are prepared by randomly positioning all the ions and neutral particles in the simulation domain and giving them Maxwell-distributed random velocities. The Newton equations of motion are integrated with the use of the leapfrog method, which is equivalent to the Verlet algorithm [26]. The unit of time is $\tau = a\sqrt{m/\epsilon}$, and we choose the integration time step $\Delta t = 0.01\tau$, where $\tau \approx 1\text{ps}$ in real environments. The simulation runs are executed well beyond the time when the dynamical property (the macroion drift speed in this study) has become stationary, and only the stationary part is used for data analysis. Under the electrostatic and Lennard-Jones forces where the random forces and frictional forces are represented by particle solvent, typical run times are between 2000τ and 4000τ (some runs are continued further to check the long term variability, but the results fall within the error bars).

As noted earlier, we can adopt the heat bath without side effects for the present study with the neu-

tral electrolyte solvent. At the center of the heat bath the macroion is located at every moment. The velocities of the neutral particles crossing the boundaries are refreshed according to the thermal distribution of the given temperature. Throughout this paper, the same normalization of the mobility $\mu_0 = v_0/(|Q_{00}|/\epsilon R_0^2) \approx 21(\mu\text{m}/\text{sec})/(\text{V}/\text{cm})$ is used, where $Q_{00} = -80e$, $R_0 = 5a$ and v_0 is the thermal speed of neutral (solvent) particles.

III. THE EFFECTS OF ASYMMETRIC COIONS/COUNTERIONS

The dependence of the electrophoretic mobility of a macroion on the ratio of coion and counterion radii a^-/a^+ is shown in Fig.1. The coion radius is varied between $0.5a$ and $2.5a$ for the fixed counterion radius $a^+ = a$, and the Bjerrum length is $\lambda_B = e^2/\epsilon k_B T = 5a$. The counterion valence is $Z^+ = 2$ (diamonds), 3 (circles) and 5 (squares). The number of monovalent coions is $N^- \sim 60$, which corresponds to the density $1.8 \times 10^{-3}/a^3 \approx 1.1$ Mol/l, and that of the counterions is determined by charge neutrality. The macroion with charge $Q_0 = -80e$ and radius $R_0 = 5a$ has the surface charge density $\sigma_{sp} \sim 0.26e/a^2$ (2.1 C/m²). The electric field is $E = 0.1\epsilon/ae \ll Q_0/\epsilon R_0^2$ which ensures that the electrophoresis occurs in the linear regime [13].

Figure 1 shows that the mobility is reversed (positive) and increases almost linearly with the ratio a^-/a^+ . The mobility peaks at the intermediate coion radius $a^-/a^+ \approx 1.5$, beyond which the mobility sharply decreases and flips to non-reversed. The degradation of the mobility does not depend on the counterion valence nor is indexed to the coion and counterion interaction energy $Z^+Z^-e^2/\epsilon(a^- + a^+)$ which is always larger than thermal energy $k_B T$ (between 5 and 10 times for $Z^+ = 3$). On the other hand, the volume fraction of the ions becomes significant, $4\pi(N^-(a^-)^3 + N^+(a^+)^3)/3L^3 \sim 0.07$ for $a^- = 2a$ and 0.13 for $a^- = 2.5a$.

The reversed mobility at $a^- = a^+$ and $Z^+ = 3$ is 12 $(\mu\text{m}/\text{sec})/(\text{V}/\text{cm})$. The experiment with a sulphonated latex particle of the surface charge density 0.115 C/m² obtained the saturated mobility 0.25 $(\mu\text{m}/\text{sec})/(\text{V}/\text{cm})$ for 50 mM/l $\text{La}(\text{NO}_3)_3$ (Fig.6 of Ref.[17]). Although exact comparison is difficult, we note that the theory predicts [10] that net charge Q^* , hence the mobility, scales as $Q^*/R_0^2 \sim \sigma(R_{WS}/\lambda_D) \sim (Ze\sigma c_s)^{1/2}$ for the weak Debye shielding regime, where $\lambda_D = (\epsilon k_B T/8\pi c_s e^2)^{1/2}$ with c_s the coion density, and $R_{WS} = (Ze/\pi\sigma_{sp})^{1/2}$ is the Wigner-Seitz cell radius. This formula may be applicable because of weak lateral screening on the macroion surface due to the absence of coions there. The mobility of the former is expected to be 37 times that of the latter, whose agreement is fair.

The cases with reversed mobility are characterized by the peaked radial distribution profile of the counterions localized on the macroion surface and strong association of coions to the counterions, as seen in Fig.2(a). The integrated charge $Q(r)$ in the inset panel is peaked and

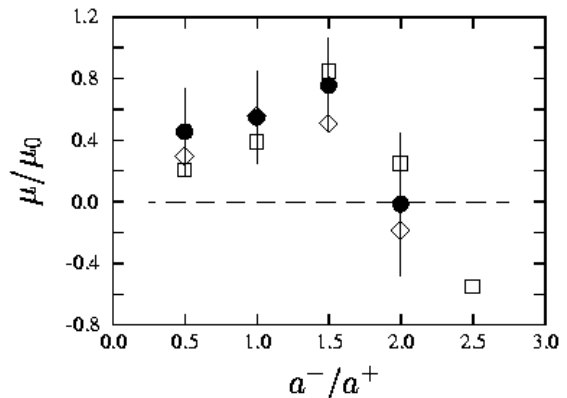


FIG. 1: The electrophoretic mobility of the macroion μ is shown against the ratio of coion and counterion radii a^-/a^+ . The counterion radius is fixed at $a^+ = a$, and their valence is $Z^+ = 2$ (diamonds), 3 (circles), and 5 (squares). The surface charge density of the macroion is $\sigma_{sp} \sim 0.26e/a^2$ (2.1 C/m²) for the charge $Q_0 = -80e$ and radius $R_0 = 5a$. Here, the normalization of the mobility is $\mu_0 = v_0/(|Q_0|/\epsilon R_0^2) \approx 21(\mu\text{m}/\text{sec})/(\text{V}/\text{cm})$ with v_0 the thermal speed of neutral particles. The number of monovalent coions is $N^- \approx 60$ (1.1Mol/l). The Bjerrum length is $\lambda_B = 5a$.

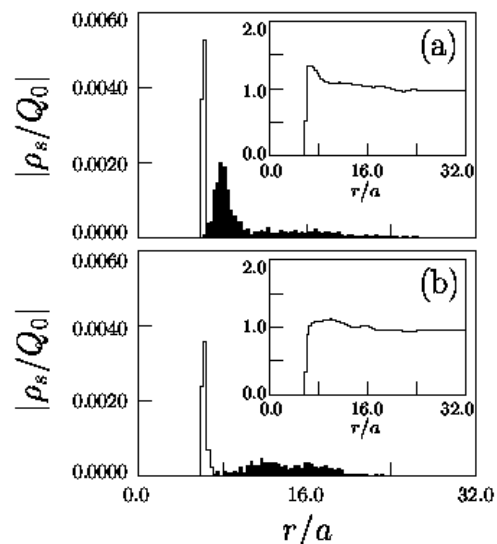


FIG. 2: The radial distribution functions of charge density ρ_s of counterions (solid bars) and coions (shaded bars), with the coion radius (a) $a^- = a$ and (b) $a^- = 2a$, are shown for the runs in Fig.1 (the coion bars are enlarged by ten times). The counterion radius is $a^+ = a$ and valence $Z^+ = 3$. The inset panels show the integrated charge distribution $Q(r)/|Q_0|$ of the corresponding counterion and coion charge densities.

larger than the neutrality $|Q_0|$. By contrast, for the case of non-reversed mobility at $a^- = 2a$ in Fig.2(b), the aggregates made of one counterion and a few condensed large coions distribute more homogeneously and apart from the macroion than for the $a^-/a^+ = 1$ case. The radial profile of the integrated charge is nearly flat due to less concentrated counterions, thus the dynamical and

static observables of charge inversion are consistent.

The increase in the mobility with coion radius arises from less amount of charge compensation by large coions due to geometrical avoidance on the counterion surface. This is consistent with the Monte Carlo simulation of charge inversion for the finite-size coions [7] and the condensation of the $Z : 1$ ions with the size asymmetry [27]. Our observation shows that the degradation of the mobility for large coions is due to collisions; a part of adsorbed counterions are kicked out of the macroion surface whose return is hampered and delayed by large coions surrounding the macroion. This is contrary to the charge inversion enhancement by the excluded volume ordering by large and symmetric coions and counterions [28].

The effect of asymmetric valences between counterions and coions on the electrophoretic mobility is shown in Fig.3. The coion valence Z^- is varied for the fixed counterion valence Z^+ which is either divalent, trivalent or tetravalent. The macroion surface charge density is $\sigma_{sp} \sim 0.26e/a^2$ (2.1 C/m^2) for the charge and radius $Q_0 \sim -80e$ and $R_0 = 5a$. The charge content carried by coions is kept the same such that $N^- = 300/Z^-$, and that of the counterions is determined by charge neutrality. The radius of the coions and counterions is equal, $a^- = a^+ = a$.

Figure 3(a) shows that the mobility is reversed and largest for the monovalent coions, i.e. for the largest asymmetry with any Z^+ value. The mobility becomes larger as the valence of the counterions increases from divalent, trivalent to tetravalent at $Z^- = 1$. As the degree of the asymmetry decreases with the increase in coion valence, the magnitude of reversed mobility decreases as $(Z^-)^{-1}$ until the two valences become nearly symmetric, $Z^+ \sim Z^-$. The mobility remains reversed for the equal valence cases except for $Z^+ = Z^- = 1$, and finally becomes non-reversed for larger coion valences. If Fig.3(a) is replotted for the coion and counterion interaction energy modified by a factor γ as in Fig.3(b), three curves of different valences Z^+ follow a master curve, where $\gamma = 1, 2$ and 2.5 for $Z^+ = 2, 3$ and 4 , respectively. The γ factor stands for the reduction of the interaction energy by enhanced screening possibly due to condensed coions to the counterions, which is actually observed.

The charge inversion for divalent counterions and coions is in line with the theory result of the HNC-MSA integral equations [14]. The radial distribution profile of the integrated charge is peaked $Q_{peak}/Q_0 \sim 1.4$, and its trailing tail oscillates periodically around the neutrality as found previously [12, 28]. Although the $Z^+ = Z^-$ case resembles the Debye screening in the sense that the ratio of the macroion, counterion and coion valences is $Q_0/Z : 1 : 1$, neither the Debye or nonlinear Poisson-Boltzmann theory is applicable due to strong electrostatic interactions and charge inversion takes place.

The dynamical results of the mobility in Fig.3 are compared with the static results in Fig.4 that depicts the radial distribution functions for trivalent counterions and the coions with (a) $Z^- = 1$ and (b) $Z^- = 3$. In the

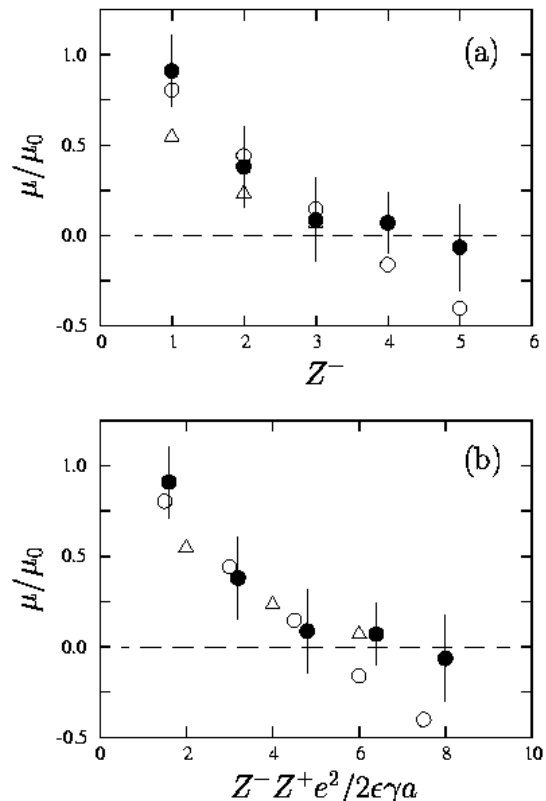


FIG. 3: The macroion mobility is shown against (a) the coion valence Z^- , and (b) the modified interaction energy of counterions and coions $Z^+Z^-e^2/2\epsilon\gamma a$, for the fixed counterion valences, $Z^+ = 2$ (triangles), $Z^+ = 3$ (open circles), and $Z^+ = 4$ (solid circles). The γ factor is 1.0, 2.0 and 2.5 for $Z^+ = 2, 3$ and 4 , respectively. Coions and counterions are of the same radius, $a^- = a^+ = a$, and the temperature is $e^2/\epsilon a k_B T = 5$ (the Bjerrum length $\lambda_B = 5a$).

panel (a), the counterions are strongly adsorbed to the macroion and the radial profile of the integrated charge in the inset panel is peaked, $|Q_{peak}/Q_0| \approx 1.6$. Both the dynamical and static observables indicate strong charge inversion. It is counterintuitive, however, that the maximum peak height of the integrated charge in Fig.4(b) is not proportional to the small mobility measured in Fig.3. The integrated charge profile with a sharp dip after the first peak is usually associated with small reversed or non-reversed mobilities. For crudely detecting the charge inversion statically, one has to count the number of the ions whose binding potential to the complex is larger than $k_B T$, which is not trivial in data analysis of the molecular dynamics simulations.

IV. SPHERICAL AND CYLINDRICAL MACROIONS UNDER MONOVALENT SALT

We study in this section both the spherical and cylindrical macroions under the monovalent salt that exists as the base component to the $Z:1$ multivalent salt. Here, the

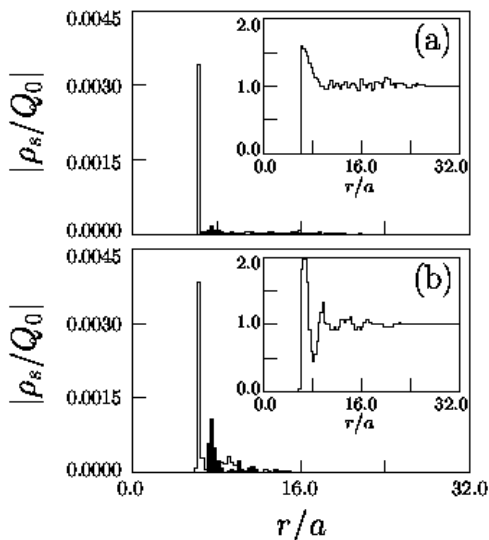


FIG. 4: The radial distribution functions of charge density ρ_s of counterions (solid bars) and coions (shaded bars), with the coion valence (a) $Z^- = 1$ and (b) $Z^- = 3$, are shown for the runs in Fig.3. The counterion valence is $Z^+ = 3$. The inset panels show the integrated charge distribution $Q(r)/|Q_0|$ of the corresponding counterion and coion charge densities.

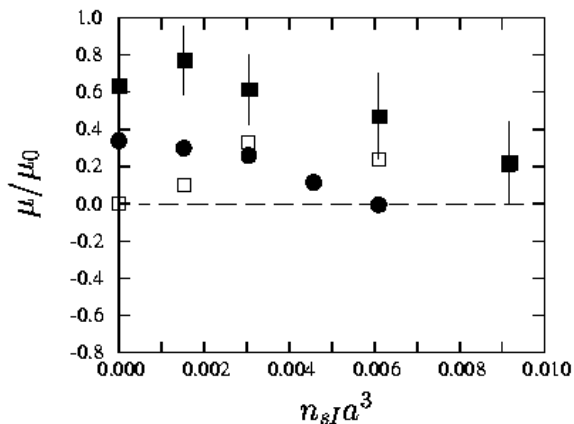


FIG. 5: The electrophoretic mobility of the spherical macroion is shown against ionic strength of monovalent salt n_{sI} (1 Mol/l salt corresponds to $0.0017/a^3$). The surface charge density of the macroion is $\sigma_{sp} = Q_0/4\pi R_0^2 \sim 0.26e/a^2$, with excess Z-ions (filled squares), and without excess Z-ions (open squares). Also, the mobility for the macroion $\sigma_{sp} \sim 0.080e/a^2$ with excess Z-ions (filled circles) is shown. Here, $\mu_0 \approx 21(\mu\text{m}/\text{sec})/(\text{V}/\text{cm})$.

trivalent counterions ($Z = 3$) are called the Z-ions, and other counterions and coions are monovalent. All these ions have equal radius $a^- = a^+ = a$.

Figure 5 shows the dependence of the mobility of a spherical macroion against ionic strength of monovalent salt, $n_{sI} = 2N^{+1}/L^3$, where N^{+1} is the number of monovalent counterions (the same number of matching monovalent coions are present). The $N^{+1} = 50$ salt ions correspond to $n_{sI} \sim 0.0031/a^3$ (1.8 Mol/l), and the Debye

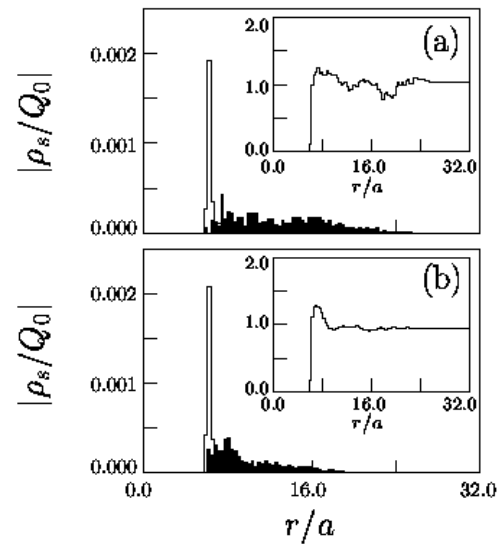


FIG. 6: The radial distribution functions of charge density ρ_s of counterions (solid bars) and coions (shaded bars) are shown for (a) the spherical macroion in Fig.5, and (b) the cylindrical macroion in Fig.8, both with surface charge density $\sigma = 0.08e/a^2$, radius $R = 5a$, and salt ionic strength $n_{sI} \sim 0.006/a^3$ (the coion bars are enlarged by three times). The inset panels show the integrated charge distribution $Q(r)/|Q_0|$ of the corresponding counterion and coion charge densities.

screening length is $1.6a$. The surface charge density for the *strongly* charged macroion with $Q_0 = -81e$ (filled and open squares) is $\sigma_{sp} \sim 0.26e/a^2$, and that for the *weakly* charged macroion with $Q_0 = -25e$ (circles) is $0.08e/a^2$ ($0.65 \text{ C}/\text{m}^2$), both with the radius $R_0 = 5a$. For these runs, the surface charge is at least several times that of the salt ions contained in the surface layer, $\sigma_{sp} \gg en_{sI}\lambda_D$. The Guoy-Chapman length is even smaller, $\lambda_{GC} = \epsilon k_B T / 2\pi Z e \sigma_{sp} \sim 0.13a$ for trivalent counterions and $\sigma_{sp} \sim 0.26e/a^2$. The Wigner-Seitz cell radius for the spherical macroion is,

$$R_{WS} = (Ze/\pi\sigma_{sp})^{1/2} = 2R_0(Ze/|Q_0|)^{1/2}. \quad (2)$$

This yields $R_{WS} \sim 1.9a$ and $3.5a$, respectively, for the *strongly* and *weakly* charged macroions in Fig.5. A series of the runs with spherical macroions of different bare charges Q_0 reveal that the charge inversion threshold under the zero monovalent salt is $Q_0 \sim 15e$ for $R_0 = 5a$. This yields $Q_0/R_0^2 \sim 0.6e/a^2$ and the surface charge density at the threshold

$$\sigma_{sp} \sim 0.048e/a^2 \quad (0.39\text{C}/\text{m}^2). \quad (3)$$

This agrees with our previous finding [13] that the threshold of surface charge density is $|Q_0|/R_0^2 \approx 0.5e/a^2$ for any combination of Q_0 and R_0 . The correlation energy of the surface Z-ions forming the Wigner-Seitz cell becomes at the threshold

$$Z^2 e^2 / 2\epsilon R_{WS} \sim 5k_B T. \quad (4)$$

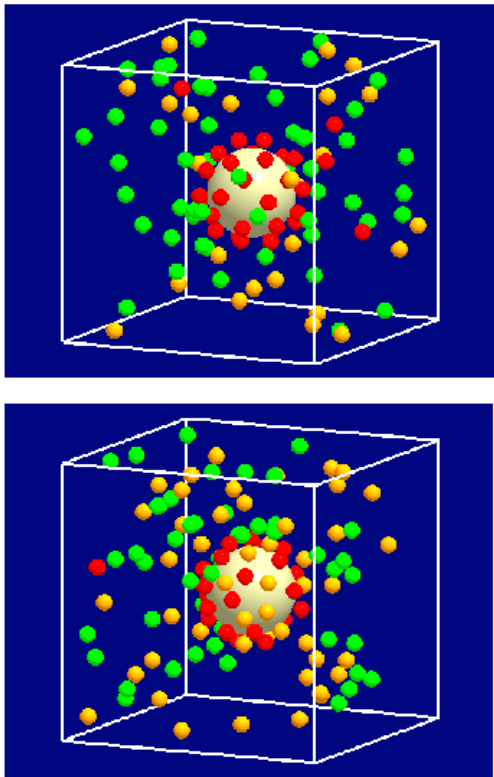


FIG. 7: The bird's-eye views of all ion species are shown for the spherical macroion with (top) and without (bottom) the excess Z-ions for the macroion of surface charge density $\sigma_{sp} \sim 0.26e/a^2$ in Fig.5. The trivalent and monovalent counterions are drawn in red and yellow, respectively, and the monovalent coions in green (nearly 4000 solvent particles are not drawn).

In Fig.5, we see that the addition of small amount of monovalent salt enhances the reversed mobility for the strongly charged macroion with excess Z-ions $N_b^{+3} = 10$ (filled squares). The mobility peaks at $n_{sI} \sim 0.0015e/a^2$ (0.83 Mol/l). However, further addition of monovalent salt whose charge concentration exceeds that of the Z-ions in the bulk screens the electric field and suppresses the charge inversion. By extrapolation, the reversed mobility is expected to terminate at $n_{sI} \sim 0.013/a^3$ (7.2 Mol/l). Even without the excess Z-ions for which $N^{+3} = |Q_0|/eZ$, the addition of monovalent salt induces the charge inversion (open squares; the fifth data point overlaps on the filled square). On the other hand, for a weakly charged macroion with excess trivalent Z-ions $N_b^{+3} = 10$, the mobility is reversed at zero salt but decreases monotonically with the salt ionic strength.

A close look at the ion distributions shows that the enhancement of the mobility at the *small* salt ionic strength in Fig.5 is due to the rearrangement of ions to achieve global energy minimization rather than the adjustment of the Z-ions on the macroion surface. This is found in the radial distribution functions of ions in Fig.6(a), and visually in the bird's-eye view plot in Fig.7. For the case with excess Z-ions, almost all the Z-ions are adsorbed to the

macroion, while monovalent salt ions including counterions are located apart from the macroion surface. For the case without the excess Z-ions, both trivalent and monovalent counterions are adsorbed to the macroion, but the coions are absent in the vicinity of the macroion. Thus, the lateral screening on the macroion surface should not be significant. The theory of charge inversion [10] predicts enhancement of overcharging by monovalent salt. However, the theory heavily relies on the screening of surface Z-ion correlations beyond the nearest neighbor cells, and the predicted overcharging occurs in the limited regime.

We interpret that the aforementioned rapid decrease in the mobility with salt ionic strength for the weakly charged macroion is due to the finite radius of the spherical macroion. Namely, a number of Z-ions adsorbed on the small surface of the macroion may not be sufficient to maintain electrostatic correlations and overcome thermal fluctuations.

Therefore, the rest of this paper is devoted to the charge inversion of a cylindrical macroion. Here, the macroion is assumed to be a rod of finite radius R_{rod} and *infinite* length, occupying the full length across the domain, and that it lies perpendicularly to the applied electric field for the ease of the simulation. It is remarked that a polyelectrolyte chain tends to align along the electric field due to the polarization effect [29]. However, the orientation of the rod may be of the second importance in the case of a non-deformable rod macroion since the counterion adsorption by the macroion is not much altered as far as the applied electric field is weak compared to the local electric field produced by the macroion, $E \ll Q_{rod}/\epsilon R_{rod}L$.

Before other results are shown, the dependence of the mobility on the length of the rod is examined. Table I summarizes the mobility for the finite length rod which has the cylinder length ℓ and is capped by two semi-spheres of radius R at each end. The surface area of the macroion is $S = 2\pi R(2R + \ell)$, and the fixed surface charge density $\sigma_{rod} \approx 0.08e/a^2$ determines the macroion charge Q_{rod} . The $\ell = 0$ case is a spherical macroion. The surface electric fields at the center and tips of the rod are thus almost the same for different rods. The mass of each rod is varied such that the ratio $Q_{rod}/M_{rod} \approx const.$ although the rod mass should not be involved in the equilibrium drift speed and the mobility. Table I shows that the mobility slightly increases for a short rod compared to the spherical macroion but becomes nearly insensitive to the length of the rod for $\ell/R_{rod} \geq 3$, if the surface charge density is maintained and the monovalent salt is not present. This rod length may indicate the transition from the 3-D to 2-D regime of the cylindrical macroion.

The charges of the *infinite rod* macroions in Fig.8 are $Q_{rod} = -80e$ (filled circles), $-60e$ (open circles) and $-40e$ (filled squares). The surface charge densities of these macroions are $\sigma_{rod} = |Q_{rod}|/2\pi R_{rod}L \sim 0.08e/a^2$, $0.06e/a^2$ and $0.04e/a^2$, respectively, which correspond to

TABLE I: The dependence of mobility μ on the length ℓ of the cylindrical macroion with the radius $R = 5a$ that lies perpendicularly to the applied electric field. The surface charge density $\sigma_{rod} \approx 0.08e/a^2$ gives the macroion charge $Q_{rod} = \sigma S$ for the surface area $S = 2\pi R(2R + \ell)$. The number of coions is $N^- \approx 90$ and monovalent salt is not present.

ℓ/a	0	5	10	15	20
S/a^2	314	471	628	785	942
$ Q_{rod} /e$	25	38	50	63	75
μ/μ_0	0.29	0.35	0.34	0.31	0.30

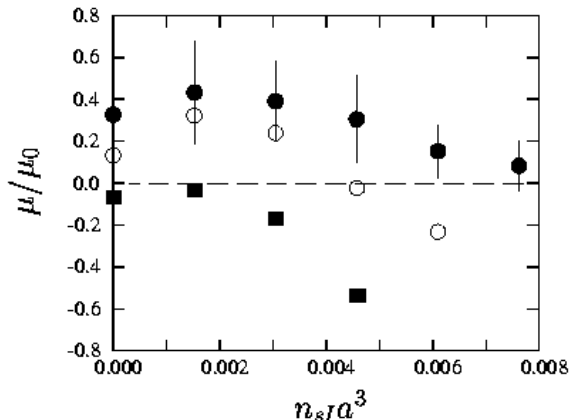


FIG. 8: The electrophoretic mobility of the rod-shaped macroion is shown against ionic strength of monovalent salt n_{sI} . The macroion is an *infinite* rod with the radius $R_{rod} = 5a$. The surface charge density of the macroion is $\sigma_{rod} \sim 0.08e/a^2$ (filled circles), $0.06e/a^2$ (open circles), and $0.04e/a^2$ (filled squares), which correspond to 0.66C/m^2 , 0.49C/m^2 and 0.33C/m^2 , respectively. The normalization of the mobility is $\mu_0 \approx 21(\mu\text{m/sec})/(\text{V/cm})$.

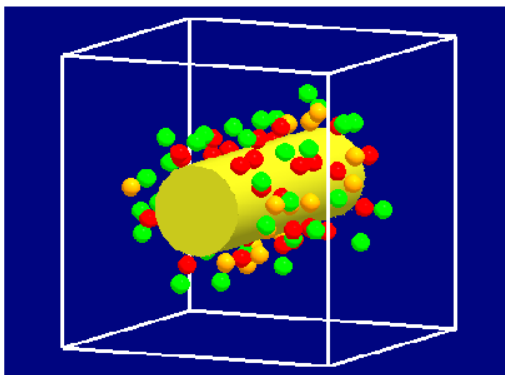


FIG. 9: The bird's-eye view of the cylindrical macroion and other ions located within $4a$ from the macroion surface are shown for the run in Fig.8. The surface charge density is $\sigma = 0.08e/a^2$ (0.66C/m^2) and the salt ionic strength is $n_{sI} \sim 0.006/a^3$ (3.6Mol/l). The trivalent and monovalent counterions are drawn in red and yellow, respectively, and the monovalent coions in green (solvent particles are not drawn).

0.66C/m^2 , 0.49C/m^2 and 0.33C/m^2 . For reference, the surface charge density of the DNA is 0.19C/m^2 . The number of Z-ions is adjusted as $N^{+3} \approx |Q_{rod}|/eZ + 30$. The Manning parameter $\xi_M = \lambda_B Q_{rod}/eL$ [30] for these rods is between 3.9 and 7.8, and counterion condensation is expected which, however, does not affect the shape of the rigid-rod macroion. We see again that the reversed mobility for the cylindrical macroion is enhanced by the addition of small amount of monovalent salt, similarly to the strongly charged spherical macroion in Fig.5. The mobility for $\sigma_{rod} = 0.08e/a^2$ is still reversed at $n_{sI} \sim 0.008/a^3$. Thus, the rod-shaped macroion is more persistent to monovalent salt than the spherical macroion of the same radius and surface charge density. The mobility of the macroion with $\sigma_{rod} = 0.04e/a^2$ is not reversed, whose surface charge density is twice large compared to that of the DNA. However, the polyelectrolyte counterions can help to overcharge the macroion [31, 32].

We compare in Fig.6 the radial distribution functions of the spherical and cylindrical macroions of Fig.5 and Fig.8 under the same condition. The surface charge density for these macroions is $\sigma \sim 0.08e/a^2$, radius $R = 5a$ and salt ionic strength $n_{sI} \sim 0.006/a^3$. The peaks of the counterion charge density are of the same height for these cases, but the marked difference is that the monovalent counterions and coions are more closely concentrated to the cylindrical macroion than to the spherical macroion. Consequently, for the latter with non-reversed mobility, two dips below the neutrality occur in the trailing tail of the integrated charge profile in Fig.6(a). For the former with reversed mobility, there is only one and well-defined peak in the integrated charge profile of Fig.6(b), which reveals strong binding of ions to the cylindrical macroion. This case is associated with a well-developed lateral network of Z-ions on the surface of the macroion, as shown in the bird's-eye view Fig.9. Majority (70%) of the Z-ions are adsorbed on this rod macroion surface, which is more than sufficient for charge neutralization. Also a small fraction (20%) of the monovalent counterions are adsorbed to the macroion, unlike the case of the spherical macroion of the same condition. Thus, the network is better packed by the counterions, which makes the surface ions less susceptible to thermal fluctuations and desorption. This supports more persistence of the rod-shaped macroion to monovalent salt than the spherical macroion of the same radius and surface charge density.

V. SUMMARY

In this paper, the charge inversion phenomenon was studied by electrophoresis, with the focuses on the effect of the asymmetric salt in size and valence, and the threshold of surface charge density of the macroion for both the spherical and cylindrical macroions. The criteria for the charge inversion obtained by the electrophoretic mobility and the radial distribution functions of ions coincided except around the charge inversion threshold.

First, large coions compared to the counterions played a positive role in enhancing the charge inversion, while the coions with larger valence than the counterions did a negative role. More specifically, the reversed mobility started at nearly null for very small coion radius, increased linearly with the ratio of the coion to counterion radii up to $a^-/a^+ \approx 1.5$. Beyond this value, the mobility decreased sharply due to large volume fraction of the coions and destruction of the complex by collisions. On the other hand, the mobility was reversed and largest for the monovalent coions, i.e. for the largest asymmetry of valences. The reversed mobility decreased with the ratio of the coion to counterion valences Z^-/Z^+ , and flipped to normal (non-reversed) for the coion valence exceeding that of the counterions. The mobility was reversed for divalent counterions and coions.

Secondly, the addition of monovalent salt enhanced reversed mobility for a strongly charged macroion at small ionic strength. This was due to global minimization of the electrolyte energy, and not only due to the local adjustment of ions on the macroion surface. On the other hand, a large amount of monovalent salt screened the electrostatic interactions and suppressed charge inversion. For a weakly charged macroion, the enhancement regime was not detected and reversed mobility decreased

monotonically with the increase in the monovalent salt concentration.

Thirdly, the threshold of surface charge density under the monovalent salt was examined. The Z-ion (multivalent counterion) correlation energy at the threshold was several times of the thermal energy, Eq.(4). A cylindrical macroion attracted counterions and coions more closely to its vicinity, formed a well packed network of the counterions, and was more persistent to the monovalent salt than the spherical macroion of the same radius and surface charge density.

Acknowledgments

The author is highly grateful to Prof.A.Yu.Grosberg for fruitful suggestions and discussions. He also thanks Prof.I.Ohmine for encouragements. The computation of the present study was performed with the Origin 3800 system of the University of Minnesota Supercomputing Institute, and the vpp800/13 supercomputer system of the Institute for Space and Astronautical Science (Japan).

-
- [1] H.G. Hindenburg de Jong, *Colloid Science, vol.2*, edited by H.R. Kruyt (Elsevier, 1949) 259-330.
- [2] E.Gonzales-Tovar, M.Lozada-Cassou, and D.J. Henderson, *J. Chem.Phys.* **83**, 361 (1985).
- [3] M.Elimelech and C.R.O'Melia, *Colloids Surface* **44**, 44, 165 (1990).
- [4] D.Bastos and F.S.De Las Nieves, *Colloid Poly. Sci.* **271**, 870 (1993).
- [5] H.W.Walker and S.B.Grant, *Colloids Surfaces A* **119**, 229 (1996).
- [6] V.A.Bloomfield, *Biopoly.* **44**, 269 (1998).
- [7] H.Greberg, and R.Kjellander, *J.Chem.Phys.* **108**, 2940 (1998).
- [8] R.R.Netz and J.F.Joanny, *Macromolecules* **32**, 9013 (1999).
- [9] W.R.Gelbart, R.Bruinsma, P.Pincus and A.Parsegian, *Physics Today* **53**, 38 (2000).
- [10] T.T.Nguyen, A.Yu. Grosberg and B.I. Shklovskii, *Phys. Rev. Lett.* **85**, 1568 (2000).
- [11] R.Messina, C.Holm and K.Kremer, *Phys.Rev.Lett.* **85**, 872 (2000).
- [12] M.Tanaka and A.Yu. Grosberg, *J.Chem.Phys.* **115**, 567 (2001).
- [13] M.Tanaka and A.Yu. Grosberg, *Euro.Phys.J., E7*, 371 (2002).
- [14] M.Lozada-Cassou, E.Gonzales-Tovar, and W.Olivares, *Phys.Rev. E* **60**, R17 (1999); M.Lozada-Cassou and E.Gonzales-Tovar, *J.Colloid Interf.Sci.* **239**, 285 (2001).
- [15] A.Yu. Grosberg, T.T. Nguyen, and B.I. Shklovskii, *Reviews Modern Phys.*, **74**, 329 (2002).
- [16] Y.Levin, *Rep.Prog.Phys.* **65**, 1577 (2002).
- [17] M.Quesada-Perez, E.Gonzalez-Tovar, A.Martin-Molina, M.Lozada-Cassou, and R.Hidalgo-Alvarez, *ChemPhysChem.* **4**, 234 (2003).
- [18] A.V.Kabanov, V.A.Kabanov, *Bioconj.Chem.*, **6**, 7 (1995).
- [19] K.Ewert, A.Ahmad, H.M.Evans, H.W.Schmidt, and C.R.Safinya, *J.Med.Chem.*, **45**, 5023 (2002).
- [20] M.Tanaka and A.Yu. Grosberg, *Bull.Amer.Phys.Soc.* **48**, 1233 (2003).
- [21] D.Long, J.-L.Viovy, and A.Ajdari, *Phys.Rev.Lett.*, **76**, 3858 (1996).
- [22] J.-L.Viovy, *Rev.Mod.Phys.* **72**, (2000) 813.
- [23] P.P.Ewald, *Ann.Physik* **64**, (1921) 253.
- [24] J.W.Eastwood and R.W.Hockney, *J.Comput.Phys.* **16**, (1974) 342.
- [25] M.Deserno and C.Holm, *J.Chem.Phys.* **109**, (1998) 7678.
- [26] D.Frenkel and B.Smit, *Understanding Molecular Simulation* (Academic Press, 1996)
- [27] A.Z.Panagiotopoulos and M.E.Fisher, *Phys.Rev.Lett.* **88**, 045701 (2002).
- [28] R.Messina, E.Gonzalez-Tovar, M.Lozada-Cassou, and C.Holm, *Europhys.Lett.*, **60**, 383 (2002).
- [29] R.R.Netz, *Phys.Rev.Lett.* **90**, 128104 (2003).
- [30] G.J.Manning, *J.Chem.Phys.* **51**, 924 (1969).
- [31] M.B.A.Silva, P.S.Kuhn and L.S.Lucena, *Physica A* **296**, 31 (2001).
- [32] S.A.Sukhishvili, O.L.Obolskii, L.V.Astafieva, A.V.Kabanov, and A.A.Yaroslavov, *Vysokomol.Soed.* **35**, 1895 (1993) [*Polymer Sci. A35*, 1602 (1993).]